Second virial coefficient of rod-shaped molecules and molecular dynamics simulations of the isotropic phase

D. M. Heyes*
Department of Physics, Royal Holloway, University of London, Egham, Surrey TW20 OEX, United Kingdom

P. Turner,† R. J. English,‡ and R. Williams§
School of Engineering & the Built Environment, Edinburgh Napier University, Merchiston Campus, 10 Colinton Road, Edinburgh EH10 5DT, United Kingdom

A. C. Brańka‖
Institute of Molecular Physics, Polish Academy of Sciences, M. Smoluchowskiego 17, 60-179 Poznań, Poland
(Received 2 February 2015; published 27 April 2015)

The second virial coefficient, B_2 is computed of linear rigid rods composed of m equally spaced sites interacting with sites on other rods via the hard-sphere or Weeks-Chandler-Andersen (WCA) pair potentials. The dependence of B_2 on a wide range of separation distance between the sites L and m for both types of potential is computed. Molecular dynamics simulations were carried out of the thermodynamic, static, and percolation properties of the WCA rigid rods in the isotropic phase as a function of rod number density ρ. Simple scaling relationships are discovered between thermodynamic and other static properties as a function of ρ and m, which extend well into the semidilute density range. The percolation threshold distance (PTD) between the centers of mass of the rods complies well with a mean-field random orientation approximation from low density well into the semidilute regime. The corresponding site-site PTD proved more problematic to represent by simple functions, but at high rod density, scales better with the number of sites density rather than the rod number density.

DOI: 10.1103/PhysRevE.91.042134 PACS number(s): 61.20.Gy, 61.20.Ja, 61.30.Cz, 61.25.he

I. INTRODUCTION

In recent years there has been growing interest in the development of novel materials derived from rod-shaped macromolecular structures such as carbon nanotubes and cellulose nanofibers. Potential applications are wide ranging, from their use as rheology modifiers, through to aerogels (with diverse properties) and high-performance structural materials. Understanding the dynamics and behavior of nanometer-scale structures in suspension forms a critical step in the development of many of these applications. The challenge links to objects, which are small enough to be strongly influenced by interacting, covariant, quantum fluctuations (vacuum energy, the suspending media and neighboring rods), which lead to an energy landscape of complex topology. Simulations of this environment at a fundamental level are for the moment computationally impractical, resulting in the need to address these challenges using some form of representative renormalization technique. Considerable effort is required if we are to understand how these rods behave and assemble in suspension under different conditions (for example, rod number density, aspect ratio, charge distribution, and ionic concentration of the suspension). A work program to resolve this should lead to a better understanding of how to control different phases (isotropic, chiral nematic, smectic, and nematic) and how these different phases can be utilised for different applications. For example, an isotropic phase is a precursor to the creation of disordered scale-free networks required to form insulating materials, while nematic alignment makes more sense for the creation of high-strength structures. A further additional benefit that could accrue from such work should be a better understanding of how macromolecular rodlike structures, such as cellulose, assemble within a plant cell wall. The goal represents a complex challenge requiring a stepwise development program. The current paper represents a first stage, addressing rod-shaped structures in the isotropic phase.

Rod-shaped particles even at relatively low volume fractions compared to spheres can have a pronounced effect on the viscosity of a colloidal liquids [1] and the strength of solid composites. Dispersions of nanocellulose rods have proved a useful model system for such investigations [2]. Despite the reduced symmetry of the particle, some aspects of its behavior can be accounted for remarkably well by simple mean-field theories, even at high concentrations. For example, the packing fraction of randomly deposited rod assemblies composed of long rods can be expressed to a high degree of accuracy in terms of the excluded volume of the rod and the mean coordination number [3–5]. Solutions of rods show an increased slope of the dependence of viscosity with density at a so-called dilute to semidilute transition. In the dilute regime the rotational motion of the rods can be considered to a good approximation to be independent of that of other rods. In the semidilute regime the rod's end-over-end motion is restricted by interaction with the other rods, which one might refer to as entanglement in analogy with the behavior of flexible polymer solutions. Both dilute and semidilute density ranges are known as isotropic phases because averaged over time there is no preferential direction for the rods to align.

*david.heyes@rhul.ac.uk
†p.turner@napier.ac.uk
‡r.english@napier.ac.uk
§r.williams@napier.ac.uk
‖branka@ifmpan.poznan.pl

If the aspect ratio of the rod (the length of the rod in units of the width) is a, for long rods, i.e., ($a \gg 1$), the dilute to semidilute transition rod number density, ρ^*, is where there is about one rod on average in a volume of $\sim a^3$ [6,7]. When the rod number density is much less than $\sim a^{-3}$ the interaction part of the equation of state can be expressed well in terms of the second virial coefficient, whereas for densities much greater than $\sim a^{-2}$ the rods are strongly entangled, and the isotropic-to-nematic transition occurs for a number density of $\sim a^{-1}$, i.e., when there are about a^2 rods per a^3 [8]. It is well known that rod-shaped particles form various liquid crystallinelike phases at high concentration, which have been been widely studied by experiment, theory, and molecular simulation [9–13]).

The fused rod systems considered here fall within the category of discrete site molecular systems, which have been treated by a number of theoretical methods that have been applied to high-density systems. These include the reference interaction site model (RISM) of Chandler and Andersen [14], which is an extension of the Ornstein-Zernike equations to a many-interaction center representation of a molecule. Recent extensions of this technique to more properly take account of excluded volume effects (i.e., 3D-RISM [15]) are reviewed in Sec. 9 of Ref. [16]. Of relevance to this work, RISM has been applied recently to tetrahedral colloidal particles, [17], homonuclear hard dumbbells [18], and m-interaction center fused rods [19]. Fundamental measure density functional (FMDFT) theory is another approach, which has been used to model elongated particles in the bulk [20–24], and confinement [25]. FMDFT has been tested for nonconvex bodies, in particular, hard dumbbells [26], which as this work is concerned with fused sphere rods is relevant to the present study. Dorosz and Schilling performed molecular dynamics simulations of crystallization of glassy suspensions of hard ellipsoids [27]. The focus here is mainly on rod assemblies at much lower concentrations, where the second virial coefficient could be considered to dominate the system thermodynamics.

There are still some qualitative and quantitative aspects of dilute rod systems, which require further elucidation. For example, over what concentration range can the second virial coefficient (B_2) term be deemed representative of the equation of state, and how does this depend on the aspect ratio? Can this information be used to provide a more objective definition of what is actually meant in terms of the system's microstructure by the terms, dilute, and semidilute regimes? This basic information is a useful foundation on which to develop more rigorous thermodynamic and rheological equations of state of rod-containing systems, as well as providing another starting point for theories of liquid crystals.

The cylinder and spherocylinder (a cylinder capped by hemispheres at both ends) representations of rods have been widely used in statistical mechanical theory and related simulations of rod-shaped particle assemblies. However, because these inter-rod interactions are discontinuous (like the hard sphere itself), certain properties are not trivial to compute numerically. Also such a discontinuous potential cannot distinguish between different types of chemical system, which requires a tunable continuous force field. A tunable anisotropic potential for high aspect ratio rods has been developed based on the Lennard-Jones (LJ) potential but it appears not to be in a suitable form for carrying out molecular simulation [28]. Representing the rod by a line of interaction sites is one way of implementing continuous interactions, although for high aspect ratio near parallel rods, side-side interactions can be computationally demanding. Nevertheless in the absence of any more optimum procedure the multisite representation of the rod is the approach adopted here. There have been many statistical, mechanical, and simulation studies of linear rods composed of m equally spaced hard-sphere interaction sites of diameter, σ (fused hard spheres) separated by distance L. The aspect ratio of the rod in the fused sphere representation is approximately, $(m-1)$ if the separation between the sites is equal to σ, the diameter of the sphere centered on each site. In the more general case, the aspect ratio is, $a \simeq L(m-1)$ for $m \gg 1$.

The second virial coefficient of fused hard spheres has been computed for $L/\sigma = 0.5$ and 1 (the so-called tangent sphere case) for rods containing up to ten sites [29]. Values of B_2 for a wider range of L, as low as 0.05 and up to 2, are reported here. The second virial coefficient values for fused rods composed of sites that interact with the continuous Weeks-Chandler-Andersen (WCA) potential [30] are also presented here as a function of the m and L values used for the hard-sphere site case. The purely repulsive WCA potential is, $\phi(r) = 4\epsilon[(\sigma/r)^{12} - (\sigma/r)^6] + \epsilon$ for $r \leqslant 2^{1/6}\sigma$, and $\phi(r) = 0$ for $r > 2^{1/6}\sigma$, where r is the distance between the sites (the potential and force are zero at $r = 2^{1/6}\sigma$). Molecular dynamics (MD) simulations have been used to calculate the equation of state in the isotropic part of the phase diagram, to compare with the virial coefficient expansion.

The percolation properties of the rods are also computed, following from the pioneering study of Balberg [31]. Percolation, the formation of an infinite cluster, has previously been studied extensively in relation to thermal and electrical conductivity, and elastic or other mechanical transitions of rods [32]. At the percolation threshold (the concentration at which percolation first occurs) changes in certain physical properties can occur. Percolation can give rise to an insulator-conductor transition [31], a change in the density dependence of the viscosity of a suspension, or even perhaps higher-order thermodynamic phase transitions [33]. Theory and Monte Carlo simulation have been used to investigate the percolation properties of nonspherical particles, such as rods [34–36], overlapping ellipsoids [37,38], prisms [39], and platelets [40]. These have been extended recently to the percolation characteristics of monodisperse and polydisperse rods [41,42], which have shown that the percolation threshold exhibits an almost inverse dependence for aspect ratios even as small as 2–3. This study investigates the percolation properties of the WCA rod model outlined above.

In Sec. II the theory associated with the computed quantities is summarized, and results discussed in Sec. III. Conclusions are made in Sec. IV.

II. THEORY

A. Second virial coefficient

The ratio of the distance between the sites to the effective diameter of the sphere centered on the site, L, can be used

to control the smoothness of the rod, and for $L \ll 1$ and for large enough m the rod represented by m interaction sites approaches the spherocylinder limit [43] (in keeping with previous literature, m is used for the number of sites in the rod, and should not be confused with the mass). For $L > 1$ the effective spheres do not overlap and for $L > 2$ hard-sphere rods can pass through the gaps between the spheres in a line along the rod. The second virial coefficient, B_2, for arbitrary m and L is defined by the integral [44]

$$\begin{aligned} B_2 &= \frac{1}{2}\left(\frac{1}{4\pi}\right)^2 \iiint \{1-\exp[-\beta\Phi(\underline{R},\Omega_1,\Omega_2)]\}\, d\underline{R}\, d\Omega_1\, d\Omega_2 \\ &= \frac{1}{8\pi} \iiint \{1-\exp[-\beta\Phi(\underline{R},\Omega_{12})]\}\, d\underline{R}\, d\Omega_{12} \\ &= \frac{1}{8\pi} \int \sin\theta\, d\theta \int d\phi \int d\underline{R}\, \{1-\exp[-\beta\Phi(\underline{R},\Omega_{12})]\}, \end{aligned} \tag{1}$$

where $\underline{R}$ is the vector between the centers of mass of the two rods, $d\underline{R}$ is the corresponding volume element, Ω_1 and Ω_2 are the solid angles defining the orientation of each rod, and $\beta = 1/k_BT$ (k_B is Boltzmann's constant and T is the temperature). The solid angle Ω_{12} is made up of the spherical polar coordinate system angles θ and ϕ. For $\Omega_{12} = \Omega_1 - \Omega_2$, the potential energy between two rods is $\Phi(\underline{R},\Omega_{12}) = \sum_\alpha \sum_\gamma \phi(r_{\alpha\gamma})$, where α and γ are the site indices on the two rods 1 and 2, respectively, and $\phi(r)$ is the site-site pair potential. The spatial or $\underline{R}$ integration was performed on a cartesian grid with $\underline{R}$ defined randomly within each voxel to reduce any systematic bias in the integration from the use of a grid. For the hard-sphere case, the term $1-\exp[-\beta\Phi(\underline{R},\Omega_{12})]$ is zero if none of the site-based spheres overlaps with another from another rod, and is equal to unity if any of the spheres making up the rod overlaps with a sphere from another rod.

A Monte Carlo method was also used to compute B_2 [45]

$$B_2 = \tfrac{1}{2}\langle 1-\exp(-\beta\Phi)\rangle / V_c, \tag{2}$$

where $\langle\cdots\rangle$ denotes an average over a number of trial insertions. One of the rods is fixed in space and orientation and the other rod's center of mass is inserted at a random position and orientation [46] within the volume V_c, which is arbitrary but must be large enough and shaped appropriately to include all possible (nonzero) interactions between the sites of the two rods in an arbitrary relative orientation. While convergence with Eq. (2) is initially more rapid than Eq. (1), the first method mentioned above ultimately gave a more precise result within a reasonable computational time. As with previous studies of B_2 of fused hard-sphere rods [29] the second virial coefficient is expressed in reduced form, $B_2^* = B_2/V_R$, where the volume of the rod $V_R = \pi\sigma^3[1+(m-1)(3L/2-L^3/2)]/6$ for $L \leqslant 1$ and $V_R = m\pi\sigma^3/6$ for $L > 1$ [29]. In the WCA potential case σ, used in V_R, is the distance parameter in the potential definition.

B. Molecular dynamics simulations

Molecular dynamics (MD) simulations were carried out on linear rigid rods each composed of m evenly spaced WCA interaction sites or beads along the length of the rod. There are N rods in a cubic simulation cell of volume V and the number density of rods is $\rho = N/V$. The purely repulsive WCA potential was used between the sites on different rods to incorporate excluded volume effects. The phase behavior of the related short linear rigid LJ chain molecules of length $m = 3$ and 5 has been determined [47], although the absence of a net attractive feature in the WCA potential excludes a critical point or liquid region; so the phase behavior of the WCA rods will be quite different to the LJ rods (perhaps apart from the high-density nematic and smectic regions where excluded volume effects will dominate). The effective hard-sphere diameter, σ_{HS} of a WCA particle at $T^* = k_BT/\epsilon$ is given by the formula, $\sigma_{HS}/\sigma = 2^{1/6}/(1+\sqrt{T^*})^{1/6}$ [48]. At the reduced temperature used in the simulations, $T^* = 1$ (the asterisk being omitted in subsequent discussion) then $\sigma_{HS} = \sigma$. The fused tangent hard-sphere case has been studied extensively for rigid rods composed of hard-sphere beads [29]. The simultaneous translational and rotational equations of motion were integrated using algorithms invented by Fincham [49–52] in the 1980s. Simulations were carried out at constant energy (NVE) and using velocity rescaling constant temperature conditions [53] giving statistically the same values for the properties reported. Production simulations were carried out on 1000 rods, typically for 10^7 time steps of 0.001 reduced time units.

The pressure tensor, $\boldsymbol{P}$, was calculated using the molecular definition [54]

$$\boldsymbol{P}V = \sum_{i=1}^{N} \frac{\underline{p}_i \underline{p}_i}{m_i} + \frac{1}{2}\sum_{i=1}^{N}\sum_{j\neq i}^{N} \underline{r}_{ij}\underline{F}_{ij}, \tag{3}$$

where $\underline{p}_i$ and m_i are the momentum and mass of rod i. The vectors, $\underline{r}_{ij}$ and $\underline{F}_{ij}$ are for the relative position and force respectively between the centers of mass of rods i and j. This obviates the need to incorporate the implicit constraint force, which would be needed if the atomic definition of the pressure tensor were used [54]. For the case of rigid rods (indeed any perfectly rigid structure representation of a molecule) the molecular pressure tensor formula is the only independent one, and there is no practical reason to use the atomic form of the pressure tensor for rigid objects, which would require the intrarod site-site forces to be determined. That bond constraints need to be included in the atomistic description of the pressure tensor was also noted in Refs. [55,56].

C. Percolation

As mentioned in the Introduction, when rods form an infinitely connected network (i.e., percolate), transitions in physical properties can occur in practical systems. Some aspects of the percolation behavior of the WCA rods are computed by MD simulation carried out in this study. The percolation characteristics of spheres have been reported extensively in the literature, which acts as a useful starting point on which to base the percolation behavior of rods. The continuum or off-lattice percolation of spheres of excluded volume diameter σ (hard core) inside a permeable shell of diameter σ_p was considered by Balberg and Binenbaum [57] and more recently in Ref. [58]. A particle is deemed to be part of a cluster if the distance from

its center to at least one other particle already in the cluster is less than or equal to σ_p. At low density the expressions for permeable spheres are accurate [58]. If excluded volume interactions are ignored between the rods and assuming random relative orientations, the relationship between the percolation distance and rod number density at percolation, ρ_p can be expressed in terms of the average coordination number per particle (historically referred to as B_c), in the form $V_a\rho_p = 2.74$, where $B_c = 2.74$. The available volume for the presence of another molecule V_a is $V_a = 4\pi\sigma_p^3/3$ in the large system size, ideal gas or perfectly permeable sphere limit; therefore $\sigma_p = (2.74 \times 3/4\pi\rho_p)^{1/3} = (0.654/\rho_p)^{1/3}$.

At higher densities where excluded volume interactions become important there are deviations from this simple limiting treatment, which are conveniently explored using MD simulation. For spheres near the freezing transition the average coordination number decreases to 1.5 (see, for example, Ref. [58] and references quoted therein) as the sphere's excluded volume takes up more of the volume, which would otherwise be available to the centers of other spheres, limiting the average number it can be in contact with. Related but inevitably more complicated considerations apply to rods at high packing fraction.

The percolation threshold distance between sites on the rods (rather than between the centers of mass) is also considered here. This is perhaps a more useful percolation definition for practical applications. It has been found previously for spheres that the percolation thresholds are relatively insensitive to system size (e.g., see Ref. [58]). Many system sizes are required to determine the percolation exponents, but these are not considered here. The percolation threshold is determined in the molecular dynamics simulations by varying the value of σ_p iteratively until on average 50% of the time steps exhibit a percolation cluster. For a relatively small periodic system the probability that a given time step exhibits a percolating cluster $p(\rho)$ has a point of inflection at a density which almost coincides with the position of the step function transition for a system of infinite size [59].

III. RESULTS AND DISCUSSION

Figure 1 shows the dependence of the (rod volume reduced) second virial coefficient B_2^* for fused hard spheres as a function of rod length or m for nearest-neighbor separations within the same rod in the range $0.05 \leqslant L \leqslant 2$, where L is in units of σ, the site-sphere diameter. This data is summarized in Table I. For $L = 0.5$ and 1 the values of B_2^* in Table I agree within a fraction of a percent with previous literature values [29]. The reduced second virial coefficient can be seen to vary linearly with m to a very good approximation, which is consistent with the large m limit of the analytic formula given in Eq. (19) of Refs. [60–62]. The numerical data is also consistent with a B_2^* value of 4 for $m = 1$, which is the analytic hard-sphere result [63]. The slope of $B_2^*(m)$ increases with the reduced bond length, L. The intercept (i.e., the $m = 0$ value of the linear regression of the data in Fig. 1) and slopes are plotted as a function of L in Fig. 2, with low-order polynomial fits to these data (the continuous curves on the figure) given in the figure caption. The fit formulas are given in the caption of Fig. 2. In the limit of $L \to 0$ and the aspect ratio, $L_e = L(m-1)$ is a constant, that is, when the rod becomes smooth, it is expected that the computed second virial coefficient will tend to the spherocylinder limiting analytic form of Onsager, $B_2 = \pi(2\sigma^3/3 + L_e\sigma^2 + L_e^2\sigma/4)$ [9,43]. Substituting the definition of L_e and dividing by the volume of the rod,

$$B_2^* = \frac{4 + 6(m-1)L + 3(m-1)^2L^2/2}{1 + 3(m-1)L/2}, \qquad (4)$$

which is the volume-reduced Onsager definition of the second virial coefficient of hard spheres cast in terms of the line-of-beads approximation used in this study. From a practical point of view L should not be too small as a computationally infeasible number m of beads would be required to attain rods of reasonably large aspect ratio to test the analytic expression adequately. A suitable compromise value of $L = 1/4$ was used. In Fig. 1 a comparison is made between B_2 from Eq. (4) and numerical calculations of the second virial coefficient using $L = 1/4$ and m up to 40 are seen to agree very well. The line denoted by b2 on the figure is the fused tangent hard-sphere formula of Williamson *et al.* [62]: $B_2^* = [(11m-3) + 3.53390\pi(m-1)^2/4]/2m$, assuming that the $L = 1$ rods are isotropically averaged. On Fig. 1, this curve is indistinguishable from that fitted to the numerical values of the reduced second virial coefficient computed in this study.

Figures 3 and 4, respectively, present the corresponding quantities for the WCA rods, which show the same trends with variation in the rod geometry parameters. For the same m and L the WCA second virial coefficients are larger than the hard-sphere ones. The percentage difference between the

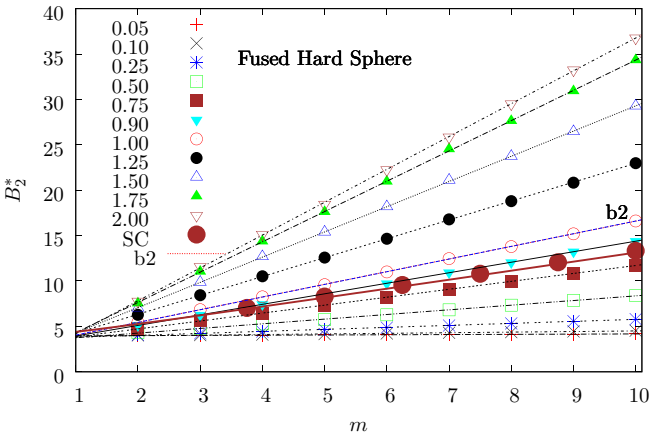

FIG. 1. (Color online) B_2^* of the fused hard sphere as a function of the number of sites in the rod, m, for a range of site-site separations, L. The solid lines are linear regressions fits, $B_2^*(L,m) = I_2(L) + S_2(L)m$, where $I_2(L)$ and $S_2(L)$ are given in the caption to Fig. 2. The red line denoted by b2 on the figure is for $L = 1$ fused hard-sphere rods using the formula of Williamson *et al.* [62]: $B_2^* = [(11m-3) + 3.53390\pi(m-1)^2/4]/2m$, which is based on mutual isotropic averaging of the orientations of the rods. This is not distinguishable from the linear fit line to the numerical data of this work, which is shown in blue. The brown line is the B_2^* spherocylinder formula given in Eq. (4), and the large brown filled in circles (labeled SC) are from numerical calculations of B_2^* using $L = 0.25$ carried out in this work. In this case, mL rather than m values are given along the abscissa, taking m up to 40.

TABLE I. Second virial coefficient B_2^* of fused hard-sphere rods. The nearest-neighbor distance L is given along the top line. The number of interaction sites in the rod, m, is given in the first column. The standard error is about 1 in the last digit.

m	L: 0.05	0.10	0.25	0.50	0.75	0.90	1.0	1.25	1.50	1.75	2.0
2	4.00	4.01	4.07	4.32	4.75	5.12	5.44	6.27	7.01	7.54	7.78
3	4.01	4.04	4.24	4.77	5.60	6.27	6.84	8.44	9.86	11.04	11.59
4	4.03	4.09	4.44	5.27	6.46	7.44	8.26	10.52	12.68	14.36	15.16
5	4.05	4.15	4.64	5.76	7.31	8.57	9.60	12.59	15.38	17.61	18.46
6	4.07	4.22	4.87	6.28	8.19	9.73	11.01	14.64	18.17	20.95	22.26
7	4.09	4.29	5.09	6.82	9.09	10.94	12.47	16.79	21.10	24.52	25.86
8	4.12	4.37	5.33	7.34	9.96	12.05	13.80	18.79	23.72	27.63	29.51
9	4.15	4.44	5.57	7.87	10.84	13.23	15.20	20.83	26.45	30.92	33.25
10	4.18	4.52	5.80	8.39	11.72	14.39	16.62	22.98	29.27	34.32	36.76

two values is largest for the shortest aspect ratio rods. For example, for $m = 2$ and $L = 0.05$, B_2^* is 4.00 and 4.48, for the hard-sphere and WCA rod types, respectively, and for $m = 10$ and $L = 0.05$, B_2^* values are 4.18 and 4.78, respectively. For $m = 2$ and $L = 2.0$, the B_2^* is 7.78 and 8.17 and for $m = 10$ and $L = 2.0$, B_2^* is 36.76 and 38.24, respectively. So for the m and L range covered, as $L \to 0$ there is about a 15% difference, and for $L = 2.0$ this becomes approximately 5%. That the second virial coefficient increases with softness for these systems is consistent with the behavior of soft sphere or $\sim r^{-n}$ particles, where $B_2(n) = 4\Gamma(1 - 3/n) > B_2(HS) = 4$. One might expect that as the rods become longer the exact details of the excluded volume term (i.e., whether hard sphere or soft sphere, for not too small n) should be less significant (as is found). This is because the configurations where the axes of two rods are near perpendicular (and therefore site-site contact is minimal) will dominate the excluded volume and hence the value of B_2.

In the definition of B_2^*, both the numerator and denominator depend on L, which obscures the L dependence of B_2 itself, and therefore a comparison between the density dependence

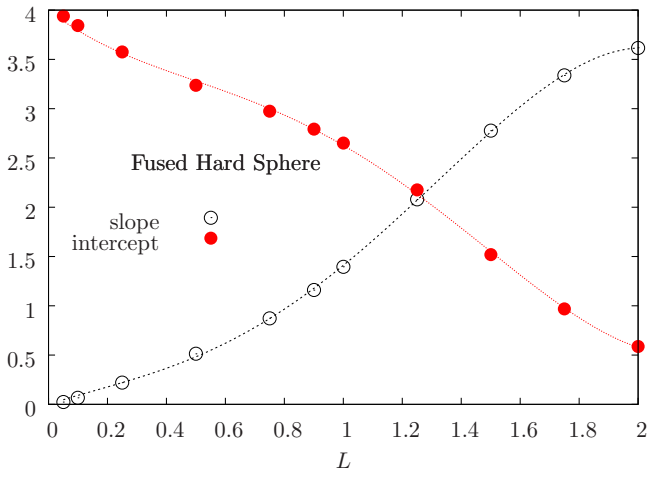

FIG. 2. (Color online) The slopes and intercepts from Fig. 1 as a function L, and their parameterized fits. For the slopes, $S_2 = a + bL + cL^2 + dL^3 + eL^4$, where $a = 0.0$, $b = 0.965982$, $c = -0.750771$, $d = 1.803303$, and $e = -0.608734$. For the intercepts (i.e., at $m = 0$), $I_2 = A + BL + CL^2 + DL^3 + EL^4$, where, $A = 4.0$, $B = -2.340471$, $C = 2.980322$, $D = -2.692036$, and $E = 0.679671$.

of the pressure from MD and the second virial coefficient is of interest. The virial expansion of the compressibility factor $Z = P/\rho k_B T = \sum_{i=1} b_i \rho^{i-1}$, where $b_1 = 1$ is a natural basis to represent the thermodynamic properties of the rod systems [29]. The configurational or interaction part of the pressure is therefore $P_c = k_B T b_2 \rho^2 + \ldots$, which can also be computed directly in the simulations from the molecular definition of the pressure tensor given in Eq. (3), using $P = (P_{xx} + P_{yy} + P_{zz})/3$ and $P_c = P - \rho k_B T$. Figure 5 presents P_c as a function of the number density of rods ρ for $m = 2$,4, and 8. The vertical arrows indicate the dilute to semidilute transition rod number density ρ^*. The lines are the corresponding equation of state from the second virial coefficient (the appropriate $L = 1$ data from Table II are used). The figure shows that the MD values for P_c at low ρ agree well with the B_2 prediction computed independently. The directly computed pressure eventually exceeds the B_2 prediction, indicating the increasing relative importance of three rod or b_3 and higher-order terms. This is at densities somewhat higher than the $\rho^* = 1/m^3$ value, which indicates that the second virial coefficient term is a good representation of the equation of state even in the semidilute region.

Figure 6 shows the projection of the rod end-to-end lines on one of the faces of the MD cell $m = 8$ close to ρ^*. The rods are instantaneously clearly not uniformly distributed but tend to cluster together in bundles, even in

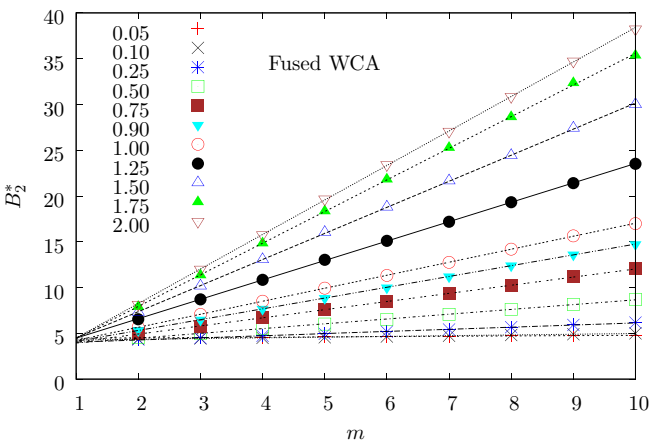

FIG. 3. (Color online) As for Fig. 1 except that the WCA rods are considered. The WCA system is considered for this and all subsequent figures.

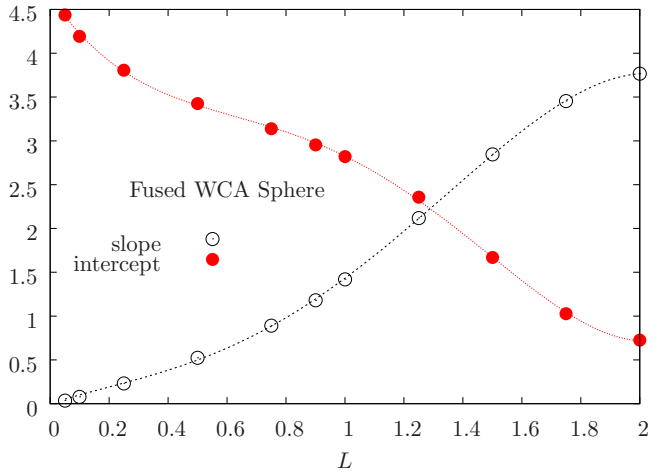

FIG. 4. (Color online) As for Fig. 2, except the WCA rods are considered. For the slopes the parameters are, $a = 0.0$, $b = 1.083934$, $c = -1.026035$, $d = 2.035387$, and $e = -0.661250$. For the intercepts the parameters are, $a = 4.654921$, $b = -4.999508$, $c = 7.504303$, $d = -5.674569$, and $e = 1.340088$.

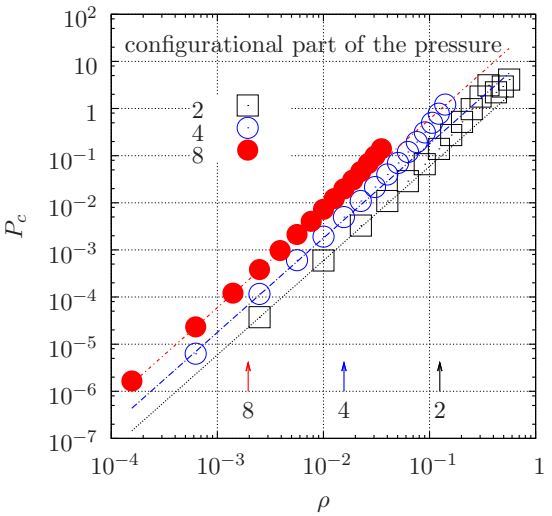

FIG. 5. (Color online) The configurational or interaction part of the pressure, P_c, as a function of the number density of rods, ρ, for $m = 2,4$, and 8, obtained by MD simulation are shown as symbols. The intersite separation in the rod is $L = 1$. The vertical arrows indicate the ρ^* for each type of rod, and from right to left going through $m = 2,4$, and 8. The lines are calculated from the equation of state up to the second virial coefficient term.

the absence of attractions. Despite the volume fraction being very low, reorientational hindrances can therefore cause the centers of mass to congregate into clusters, and therefore the isotropic phase is not instantaneously translationally uniform in certain regions. Locally in space and time the rods can be orientationally ordered. These are presumably temporary associations, and their effects on the equation of state after time averaging, are minimal however, as evident in Fig. 5. The cluster aggregation observed in Fig. 6 closely resembles the early stage formation of a percolative network, typical of a hydrogel (a precursor to the production of an aerogel). It is also indicative of the assembly of cellulose nanofibrils typically reported in the primary wall of a xylem cell found in woody plants [64].

The single rod orientational velocity $C_1(t) = \langle \underline{e}(0).\underline{e}(t) \rangle$ and angular velocity $C_\omega(t) = \langle \underline{\dot{e}}(0).\underline{\dot{e}}(t) \rangle$ autocorrelation functions were computed, where $\underline{e}$ is the unit vector along the rod and t is time ($\langle \cdots \rangle$ represents a molecule, time origin, and time average) [65]. Figure 7 shows these two functions in normalized form for two rod number densities of $1/m^3$ (the dilute-to-semidilute transition) and $1/m^2$ (the semidilute-to-concentrated transition) for $m = 8$. Time is in units of the free rotator reorientational time $\tau_r = (I/k_BT)^{1/2}$, where I is the moment of inertia of the rod. The negative or recoil regions for both functions at $t \sim 2\tau_r$ indicate that there is a gradual increase with density of the extent of entanglement of the rods. The direction changes more slowly than the angular rotational velocity, all more or less on a time scale slightly larger than τ_r [65]. This translational-rotational coupling is a subject that has been investigated by molecular dynamics simulation before (e.g., see Ref. [66]).

Can the equation of state of the isotropic phase be represented by an alternative formulation that is potentially more closely related to the geometry and smoothness of the rod? Figure 8 shows that the configurational part of the pressure P_c scales quite well with $\sim m^{1.6}$. There is a reasonably good collapse of the P_c data for $m = 2,4$, and 8 for an extensive density range, well above the dilute to semidilute crossover value (ρ^*). This might suggest that at low densities certain geometrical arrangements of the two rods (such as where the rods are essentially perpendicular) dominate the excluded volume, and hence B_2. In fact, Rickayzen and coworkers, [67] developed simple models for liquid crystals based on a set of

TABLE II. As for Table I except that the second virial coefficient B_2^* of fused WCA rods are given.

m	L: 0.05	0.10	0.25	0.50	0.75	0.90	1.0	1.25	1.50	1.75	2.0
2	4.48	4.37	4.33	4.53	4.95	5.34	5.66	6.54	7.31	7.891	8.17
3	4.55	4.44	4.50	4.99	5.80	6.48	7.07	8.71	10.17	11.35	12.01
4	4.59	4.50	4.73	5.51	6.69	7.67	8.51	10.84	13.06	14.83	15.77
5	4.61	4.57	4.94	6.01	7.57	8.85	9.94	13.04	16.02	18.34	19.68
6	4.65	4.65	5.17	6.53	8.44	10.00	11.32	15.10	18.79	21.81	23.43
7	4.69	4.74	5.42	7.08	9.35	11.21	12.76	17.19	21.66	25.27	27.08
8	4.72	4.82	5.67	7.61	10.27	12.41	14.20	19.32	24.43	28.62	30.87
9	4.75	4.91	5.92	8.15	11.17	13.60	15.64	21.42	27.41	32.34	34.73
10	4.78	5.00	6.18	8.70	12.03	14.73	16.99	23.52	30.00	35.35	38.24

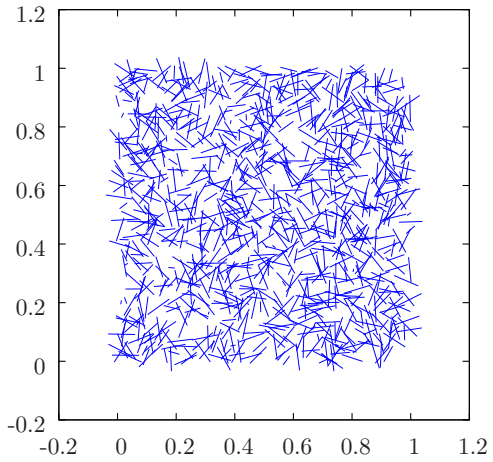

FIG. 6. (Color online) Projection of the rod end-to-end lines on one of the faces of the MD cell for a rod parameter, $m = 8$ and $\rho = 0.002 \simeq \rho^*$. The intersite separation in the rod is $L = 1$.

a few dominant relative orientations of the long molecules, an approximation, which may therefore be useful in describing the isotropic phase. Figure 9 shows the potential energy per site, u_s, which also shows good scaling with respect to a fractional power of m, in this case as $m^{1.45}$. Figures 10 and 11 show the corresponding mean square force, and torque on a rod, respectively, scaled by powers of m to collapse the different rod length data onto a single curve, to a good approximation at low density.

Figure 12 presents the atom-atom (AA) and center of mass (COM) to center of mass (RR) radial distribution functions $g(r)$ for $m = 8$ rods at two values of ρ. Two ρ values are considered, $\rho = 0.013$ in the bottom frame, and 0.063 in the top frame. For this m the crossover density $\rho^* = 0.0019$.

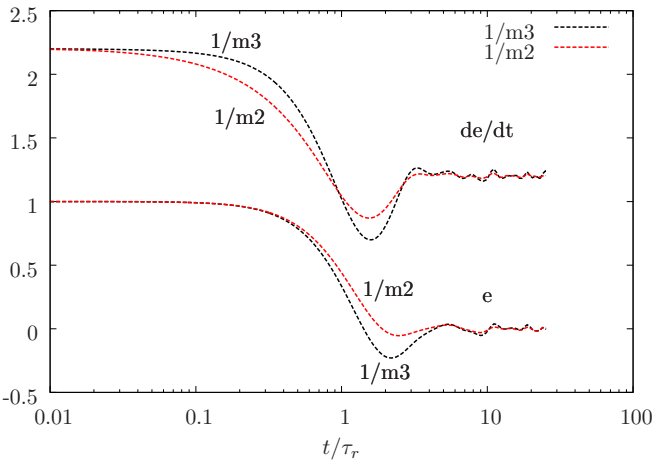

FIG. 7. (Color online) Single rod orientational, $C_1(t) = \langle \underline{e}(0).\underline{e}(t)\rangle$ and angular velocity $C_\omega(t) = \langle \dot{\underline{e}}(0).\dot{\underline{e}}(t)\rangle$ autocorrelation functions are shown for two rod number densities, $1/m^3$ (dilute-to-semidilute) and $1/m^2$ (semidilute-to-concentrated transition), where $m = 8$. Time is in units of the free rotator reorientational time τ_r. The rod number densities, $\rho = \rho^* = 1/m^3$ and $1/m^2$. C_ω is shifted upwards by 1.2 to enable the two functions to be distinguished.

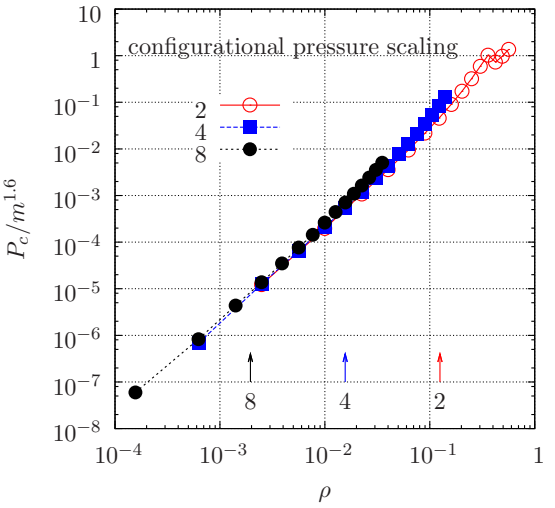

FIG. 8. (Color online) $P_c/m^{1.6}$, where P_c is the configurational or interaction part of the pressure, as a function of the number density of rods, ρ for $m = 2,4$, and 8. The vertical arrows indicate the crossover density ρ^* for each type of rod.

The two states are therefore 7 and 33 times larger than ρ^* (the latter is just below the estimated isotropic-nematic transition of $\rho_{IN} \simeq m^{-2} = 0.016$). At the lower density both types of $g(r)$ ascend quite slowly on the length scale of the rod. At the higher density site-site excluded volume interactions dominate, as both $g(r)$ superimpose for the smaller r part of the first peak, indicating significant alignment of the rods.

Figure 13 shows the percolation distance, σ_p, between the centers of mass of rods as a function of ρ for $L = 1$, computed in the MD simulations, as the symbols on the graph. The solid line A on the figure is the low-density permeable sphere approximation (PSA) $\sigma_p = (0.654/\rho)^{1/3}$. The continuous line labeled B on the figure includes more exact excluded volume corrections using the semiempirical

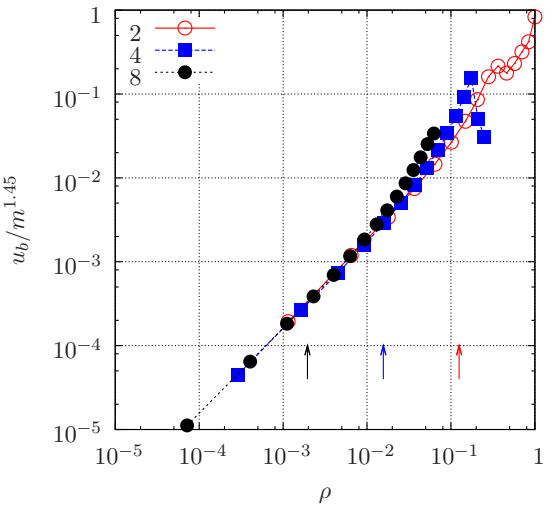

FIG. 9. (Color online) As for Fig. 8 except that the potential energy per bead, $u_b/m^{1.45}$ is shown as a function of the number density of rods, ρ for $m = 2,4$, and 8. The vertical arrows indicate ρ^* for each type of rod.

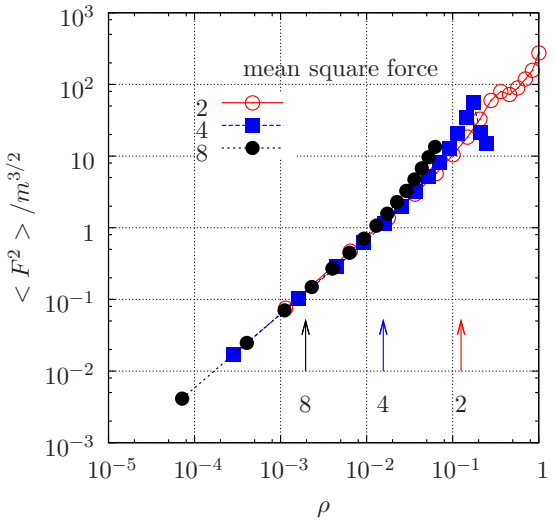

FIG. 10. (Color online) As for Fig. 9 except the mean square force on the center of mass, F^2 is plotted divided by $m^{3/2}$.

formula in Eq. (9) substituted in Eq. (6) for σ_p given in Ref. [58]. The center-of-mass percolation data presented in the figure is mainly for 1000 rods. Some points for 216 rods, also given on the figure, are seen to be indistinguishable from the $N = 1000$ data.

This curve only departs from the low-density hard-sphere approximation in the bottom right-hand corner of the figure for rod number densities in excess of about 0.1. The figure demonstrates that PSA accounts very well for the percolation distance between the COM of the rods far into the semidilute regime. This excellent agreement, better than might reasonably have been expected, indicates the averaging out of orientational correlation effects between different rods, while the centers of mass points conform to a dilute gas statistical distribution. This approximation is at the center of other mean-field theories of randomly assembled rod assemblies [5].

Figure 14 presents the corresponding atom-atom percolation distance σ_p versus ρm. The σ_p data for the three rod

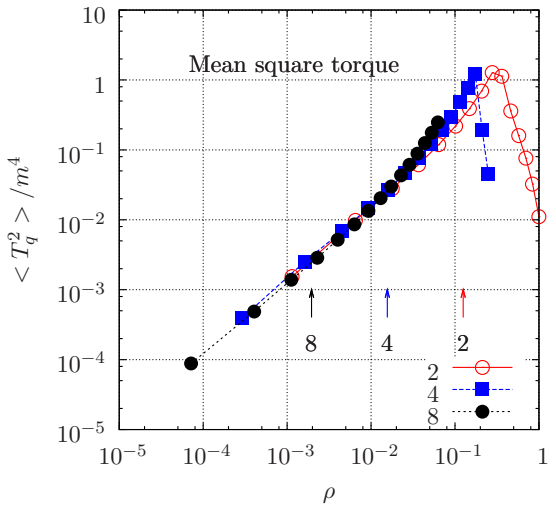

FIG. 11. (Color online) As for Fig. 10 except the mean square torque on each rod, $\langle T_q^2 \rangle / m^4$ is plotted.

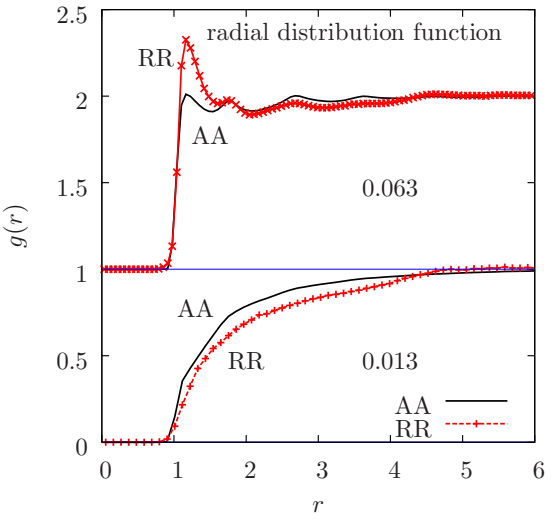

FIG. 12. (Color online) Radial distribution function, $g(r)$, between the beads or atoms along the $m = 8$ rod (AA), neglecting the intramolecular terms, and between the centers of mass of the rods (RR). Two ρ values are considered; bottom frame $\rho = 0.013$ and top frame, $\rho = 0.063$, where $\rho^* \equiv m^{-3} = 0.00195$. The $g(r)$ for the higher density are shifted upwards by 1 for clarity.

lengths collapse reasonably well onto a single curve, at least at high density, better using the number density of sites (i.e., ρm) rather than that of the rods. This is perhaps not unexpected as

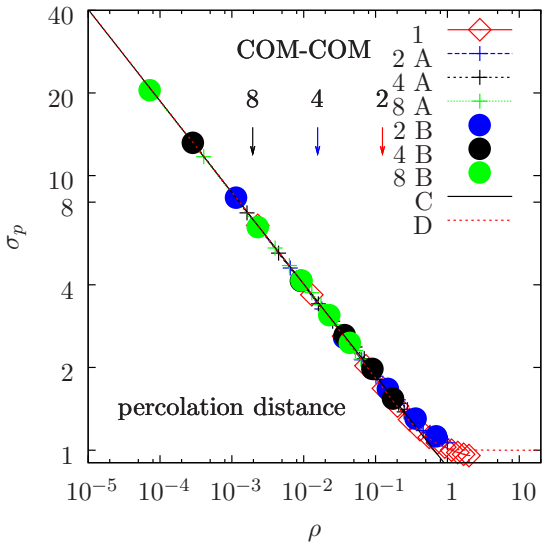

FIG. 13. (Color online) The percolation distance between the centers of mass of rods containing two, four, and eight sites plotted as a function of ρ. Most of the points are for $N = 1000$ rods (A) and a few (the larger symbols) are for $N = 216$ (B). Key: The solid line, C, on the figure is the low-density approximation, which gives, $\sigma_p/\sigma = (0.654/\rho_p)^{1/3}$, where ρ_p is the number density of rods or percolation threshold for the connectivity distance, σ_p, and line, D, is a development of A, including excluded volume corrections as described in Ref. [58]. The formula in Eq. (9) in that work is substituted in Eq. (6) of the same work, using the definition for the permeable sphere packing fraction, $\zeta \equiv \pi\rho_p/6$. The vertical arrows on the figure indicate ρ^* for the three m values. Note the log-log scale.

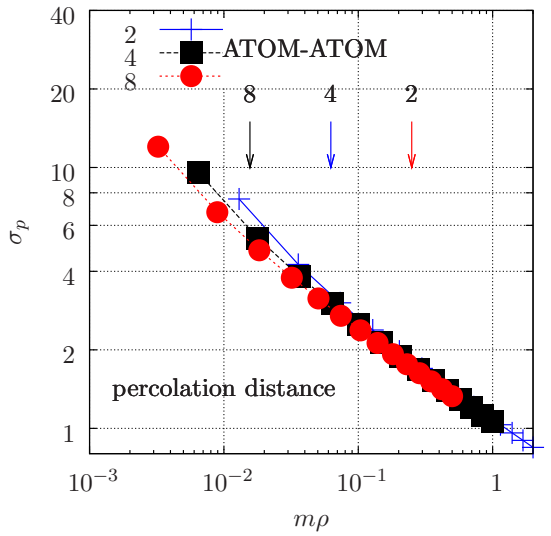

FIG. 14. (Color online) The percolation distance between the atoms of rods containing two, four, and eight sites plotted as a function of the site number density $m\rho$. The vertical arrows indicate the ρ^*.

the dominant length scale in this rod density regime will be the intersite distance rather than the length of the rod (analogous to some extent with the importance for some properties of the distance between entanglements rather than the polymer chain length in polymer melts). There is convergence of the atom-atom σ_p towards unity in the high-density excluded volume dominated limit, which can be lower than σ because of the softness of the WCA potential. At low average site number density ρm, the percolation distance is larger for the longer rods because the distribution of sites is less uniform in space when parcelled into compact units of m.

IV. CONCLUSIONS

To summarize, a number of gaps in the existing literature of fused sphere rods are filled in the present study. A wider range of bond lengths is considered than in previous studies, for rods containing up to ten interaction sites. Hard sphere and soft fused sphere rods, in the form of the Weeks-Chandler-Andersen (WCA) continuous interaction are explored and compared. The second virial coefficients in rod volume reduced form B_2^* as a function of the number sites in the rod m and bond length L are calculated and fitted to simple polynomial expressions. The differences (in percentage terms) in the B_2^* values between the two potential forms are most pronounced for small L and m, with the WCA quantity being always larger. The second virial coefficient in the WCA case is a good representation of the equation of state well into the semidilute regime. The appearance of deviations from this behavior might serve as a more physically meaningful crossover density into a domain in which three-body interactions and caging effects make a significant contribution to the physical properties. This is below the isotropic-nematic transition density. The percolation distance between the centers of mass of the rods was found to follow the permeable sphere mean-field model well into the semidilute regime. This indicates that for this static property at least, the orientational degrees of freedom couple weakly to the translational ones in the isotropic region of the phase diagram. As a more theoretically transparent and computationally efficient model in future studies there may be advantages in adopting a single site pair potential between the rods, e.g., as for square well rods [68].

As stated at the outset, this work represents a first step in a program to consider the phase behavior of rod-shaped macromolecules in suspension. A considerable amount of additional work is needed to support our understanding of the more complex isotropic-nematic transition. This will require the inclusion of an extended range of variables into simulations such as higher rod number density ranges, ionic concentration of the suspending media, and charge density and its distribution on a rod. Such a program will need to go hand in hand with experimental work to fine tune and validate the models. The objective is to fill important gaps in our understanding of empirically observed phenomena at the nanometer scale, offering new insights into the conditions required to manipulate and control the assembly of rod-shaped macromolecules used in the manufacture of materials. It is hoped that it may also offer new insights into the mechanisms used by plants to control cellulose nanofiber assembly to create the diverse array of structures observed.

ACKNOWLEDGMENTS

D.M.H. thanks Edinburgh Napier University, where the early stages of this work were carried out, for financial support.

[1] A. V. Kyrylyuk and P. van der Schoot, Proc. Nat. Acad. Sci. USA **105**, 8221 (2008).
[2] X. M. Dong, T. Kimura, J.-F. Revol, and D. G. Gray, Langmuir **12**, 2076 (1996).
[3] A. P. Philipse, Langmuir **12**, 1127 (1996).
[4] S. R. Williams and A. P. Philipse, Phys. Rev. E **67**, 051301 (2003).
[5] A. Wouterse, S. Luding, and A. P. Philipse, Gran. Matt. **11**, 169 (2009).
[6] M. Doi and S. F. Edwards, J. Chem. Soc. Farad. Trans. 2 **74**, 560 (1978).
[7] M. Doi and S. F. Edwards, J. Chem. Soc. Farad. Trans. 2 **74**, 918 (1978).
[8] Z. Y. Chen, Macromol. **26**, 3419 (1993).
[9] L. Onsager, Ann. N.Y. Acad. Sci. **51**, 627 (1949).
[10] D. Frenkel, J. Phys. Chem. **92**, 3280 (1988).
[11] P. Bolhuis and D. Frenkel, J. Chem. Phys. **106**, 666 (1997).
[12] P. A. Buining and H. N. W. Lekkerkerker, J. Phys. Chem. **97**, 11510 (1993).
[13] M. Bercea and P. Navard, Macromol. **33**, 6011 (2000).
[14] D. Chandler and H. C. Andersen, J. Chem. Phys. **57**, 1930 (1972).

[15] D. Beglov and B. Roux, J. Phys. Chem. B **101**, 7821 (1997).
[16] J. Ram, Phys. Rep. **538**, 121 (2014).
[17] G. Munaò, D. Costa, F. Sciortino, and C. Caccamo, J. Chem. Phys. **134**, 194502 (2011).
[18] G. Munaò, D. Costa, and C. Caccamo, J. Chem. Phys. **130**, 14504 (2009).
[19] P. González-Mozuelos, J. M. Médez-Alcarez, and R. Castañeda-Priego, J. Chem. Phys. **123**, 214907 (2005).
[20] H. Hansen-Goos and K. Mecke, Phys. Rev. Lett. **102**, 018302 (2009).
[21] H. Hansen-Goos and K. Mecke, J. Phys. Cond. Matt. **22**, 364107 (2010).
[22] M. Marechal, S. Korden, and K. Mecke, Phys. Rev. E **90**, 042131 (2014).
[23] A. Härtel and H. Löwen, J. Phys. Cond. Matt. **22**, 104112 (2010).
[24] R. Wittmann, M. Marechal, and K. Mecke, Euro. Phys. Lett. **109**, 26003 (2015).
[25] H. H. Wensink, H. Löwen, M. Marechal, A. Härtel, R. Wittkowski, U. Zimmermann, A. Kaiser, and A. M. Menzel, Eur. Phys. J. Special Topics **222**, 3023 (2013).
[26] M. Marechal, H. H. Goetze, A. Härtel, and H. Löwen, J. Chem. Phys. **135**, 234510 (2011).
[27] S. Dorosz and T. Schilling, J. Chem. Phys. **139**, 124508 (2013).
[28] F. J. Vesely, J. Chem. Phys. **125**, 214106 (2006).
[29] T. Boublik, J. Chem. Phys. **119**, 7512 (2003).
[30] H. C. Andersen, J. D. Weeks, and D. Chandler, Phys. Rev. A **4**, 1597 (1971).
[31] I. Balberg, J. Phys. D: Appl. Phys. **42**, 064003 (2009).
[32] R. C. Picu, Soft. Matter **7**, 6768 (2011).
[33] K. W. Kratky, J. Stat. Phys. **52**, 1413 (1988).
[34] I. Balberg, N. Binenbaum, and N. Wagner, Phys. Rev. Lett. **52**, 1465 (1984).
[35] Z. Néda, R. Florian, and Y. Brechet, Phys. Rev. E **59**, 3717 (1999).
[36] L. Berhan and A. M. Sastry, Phys. Rev. E **75**, 041120 (2007).
[37] E. J. Garboczi, K. A. Snyder, J. F. Douglas, and M. F. Thorpe, Phys. Rev. E **52**, 819 (1995).
[38] G. Ambrosetti, N. Johner, C. Grimaldi, A. Danani, and P. Ryser, Phys. Rev. E **78**, 061126 (2008).
[39] M. O. Saar and M. Manga, Phys. Rev. E **65**, 056131 (2002).
[40] M. Mathew, T. Schilling, and M. Oettel, Phys. Rev. E **85**, 061407 (2012).
[41] A. P. Chatterjee, J. Phys.: Condens. Matt. **20**, 255250 (2008).
[42] B. Nigro, C. Grimaldi, P. Ryser, A. P. Chatterjee, and P. van der Schoot, Phys. Rev. Lett. **110**, 015701 (2013).
[43] H. Graf and H. Löwen, J. Phys.: Condens. Matter **11**, 1435 (1999).
[44] G. J. Vroegge and H. N. W. Lekkerkerker, Rep. Progr. Phys. **55**, 1241 (1992).
[45] H. Fynewever and A. Yethiraj, J. Chem. Phys. **108**, 1636 (1998).
[46] M. P. Allen and D. J. Tildesley, *Computer Simulation of Liquids* (Clarendon Press, Oxford, 1987), p. 349.
[47] A. Galindo, C. Vega, E. Sanz, L. G. MacDowell, E. de Miguel, and F. J. Blas, J. Chem. Phys. **120**, 3957 (2004).
[48] D. M. Heyes and H. Okumura, J. Chem. Phys. **124**, 164507 (2006).
[49] D. Fincham: Daresbury Lab. Information Quarterly for Computer Simulation of Condensed Phases **12**, 43 (1984).
[50] D. Fincham, Mol. Sim. **8**, 165 (1992).
[51] D. Fincham, Mol. Sim. **11**, 79 (1993).
[52] D. Fincham, N. Quirke, and D. J. Tildesley, J. Chem. Phys. **84**, 4535 (1986).
[53] S. Nosé, Progr. Theor. Phys. **103**, 1 (1991).
[54] K. P. Travis, P. J. Daivis, and D. J. Evans, J. Chem. Phys. **103**, 1109 (1995).
[55] T. Mülders, S. Tøxvaerd, and G. R. Kneller, Phys. Rev. E **58**, 6766 (1998).
[56] W. Smith and P. M. Rodger, http://www.ccp5.ac.uk/infoweb/knowledge_center/.
[57] I. Balberg and N. Binenbaum, Phys. Rev. A **35**, 5174 (1987).
[58] D. M. Heyes, M. Cass, and A. C. Brańka, Mol. Phys. **104**, 3137 (2006).
[59] D. Staufer, *Introduction to Percolation Theory* (Taylor & Francis, London, 1985).
[60] W. G. Chapman, G. Jackson, and K. E. Gubbins, Mol. Phys. **65**, 1057 (1988).
[61] C. M. McBride, C. Vega, and L. G. MacDowell, Phys. Rev. E **64**, 011703 (2001).
[62] D. C. Williamson and G. Jackson, J. Chem. Phys. **108**, 10294 (1998).
[63] J.-P. Hansen and I. R. McDonald, *Theory of Simple Liquids* (Academic Press, Amsterdam, 2006), 3rd ed., p. 32.
[64] P. Turner, M. Kowalczyk, and A. Reynolds, *New insights into the micro-fibril architecture of the wood cell wall*, COST Action E54 Book (COST Office, Brussels, Belgium, 2011).
[65] J. O'Dell and B. J. Berne, J. Chem. Phys. **63**, 2376 (1975).
[66] W. A. Steele, Mol. Phys. **40**, 723 (1980).
[67] G. Rickayzen and M. Calleja, Mol. Phys. **90**, 869 (1997).
[68] S. Varga and F. J. Vesely, J. Chem. Phys. **131**, 194506 (2009).